Decoding, Calibration and Rectification for Lenselet-Based Plenoptic Cameras

Donald G. Dansereau, Oscar Pizarro and Stefan B. Williams
Australian Centre for Field Robotics; School of Aerospace, Mechanical and Mechatronic Engineering
University of Sydney, NSW, Australia
{d.dansereau, o.pizarro, s.williams}@acfr.usyd.edu.au

Abstract

Plenoptic cameras are gaining attention for their unique light gathering and post-capture processing capabilities. We describe a decoding, calibration and rectification procedure for lenselet-based plenoptic cameras appropriate for a range of computer vision applications. We derive a novel physically based 4D intrinsic *matrix relating each recorded pixel to its corresponding ray in 3D space. We further propose a radial distortion model and a practical objective function based on ray reprojection. Our 15-parameter camera model is of much lower dimensionality than camera array models, and more closely represents the physics of lenselet-based cameras. Results include calibration of a commercially available camera using three calibration grid sizes over five datasets. Typical RMS ray reprojection errors are 0.0628, 0.105 and 0.363 mm for 3.61, 7.22 and 35.1 mm calibration grids, respectively. Rectification examples include calibration targets and real-world imagery.*

1. Introduction

Plenoptic cameras [17] measure both colour and geometric information, and can operate under conditions prohibitive to other RGB-D cameras, e.g. in bright sunlight or underwater. With increased depth of field and light gathering relative to conventional cameras, and post-capture capabilities ranging from refocus to occlusion removal and closed-form visual odometry [1, 16, 4, 9, 19, 6], plenoptic cameras are poised to play a significant role in computer vision applications. As such, accurate plenoptic calibration and rectification will become increasingly important.

Prior work in this area has largely dealt with camera arrays [20, 18], with very little work going toward the calibration of lenselet-based cameras. By exploiting the physical characteristics of a lenselet-based plenoptic camera, we impose significant constraints beyond those present in a multiple-camera scenario. In so doing, we increase the robustness and accuracy of the calibration process, while simultaneously decreasing the complexity of the model.

In this work we present a novel 15-parameter plenoptic camera model relating pixels to rays in 3D space, including a *4D intrinsic* matrix based on a projective pinhole and thin-lens model, and a radial direction-dependent distortion model. We present a practical method for decoding a camera's 2D lenselet images into 4D light fields without prior knowledge of its physical parameters, and describe an efficient projected-ray objective function and calibration scheme. We use these to accurately calibrate and rectify images from a commercially available Lytro plenoptic camera.

The remainder of this paper is organized as follows: Section 2 reviews relevant work; Section 3 provides a practical method for decoding images; Section 4 derives the 4D intrinsic and distortion models; Section 5 describes the calibration and rectification procedures; Section 6 provides validation results; and finally, Section 7 draws conclusions and indicates directions for future work.

2. Prior Work

Plenoptic cameras come in several varieties, including mask-based cameras, planar arrays, freeform collections of cameras [13, 22, 21, 18], and of course lenticular array-based cameras. The latter include the "original" plenoptic camera as described by Ng et al. [17], with which the present work is concerned, and the "focused" plenoptic camera described by Lumsdaine and Georgiev [14]. Each camera has unique characteristics, and so the optimal model and calibration approach for each will differ.

Previous work has addressed calibration of grids or freeform collections of multiple cameras [20, 18]. Similar to this is the case of a moving camera in a static scene, for which structure-from-motion can be extended for plenoptic modelling [12]. These approaches introduce more degrees of freedom in their models than are necessary to describe the lenselet-based plenoptic camera. Our work introduces a more constrained intrinsic model based on the physical properties of the camera, yielding a more robust, physically-grounded, and general calibration.

1063-6919/13 $26.00 © 2013 IEEE
DOI 10.1109/CVPR.2013.137

IEEE computer society

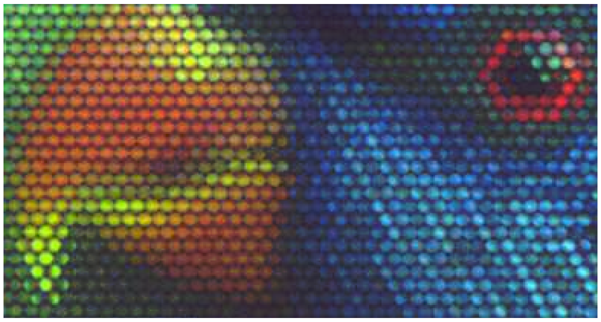

Figure 1. Crop of a raw lenselet image after demosaicing and without vignetting correction; pictured is a rainbow lorikeet

In other relevant work, Georgiev et al. [7] derive a plenoptic camera model using ray transfer matrix analysis. Our model is more detailed, accurately describing a real-world camera by including the effects of lens distortion and projection through the lenticular array. Unlike previous models, ours also allows for continuous variation in the positions of rays, rather than unrealistically constraining them to pass through a set of pinholes.

Finally, our ray model draws inspiration from the work of Grossberg and Nayar [8], who introduce a generalized imaging model built from virtual sensing elements. However, their piecewise-continuous pixel-ray mapping does not apply to the plenoptic camera, and so our camera model and calibration procedure differ significantly from theirs.

3. Decoding to an Unrectified Light Field

Light fields are conventionally represented and processed in 4D, and so we begin by presenting a practical scheme for decoding raw 2D lenselet images to a 4D light field representation. Note that we do not address the question of demosaicing Bayer-pattern plenoptic images – we instead refer the reader to [23] and related work. For the purposes of this work, we employ conventional linear demosaicing applied directly to the raw 2D lenselet image. This yields undesired effects in pixels near lenselet edges, and we therefore ignore edge pixels during calibration.

In general the exact placement of the lenselet array is unknown, with lenselet spacing being a non-integer multiple of pixel pitch, and unknown translational and rotational offsets further complicating the decode process. A crop of a typical raw lenselet image is shown in Fig. 1 – note that the lenselet grid is hexagonally packed, further complicating the decoding process. To locate lenselet image centers we employ an image taken through a white diffuser, or of a white scene. Because of vignetting, the brightest spot in each white lenselet image approximates its center.

A crop of a typical white image taken from the Lytro is shown in Fig. 7a. A low-pass filter is applied to reduce sensor noise prior to finding the local maximum within each lenselet image. Though this result is only accurate to the nearest pixel, gathering statistics over the entire image mitigates the impact of quantization. Grid parameters are estimated by traversing lenselet image centers, finding the mean horizontal and vertical spacing and offset, and performing line fits to estimate rotation. An optimization of the estimated grid parameters is possible by maximizing the brightness under estimated grid centers, but in practice we have found this to yield a negligible refinement.

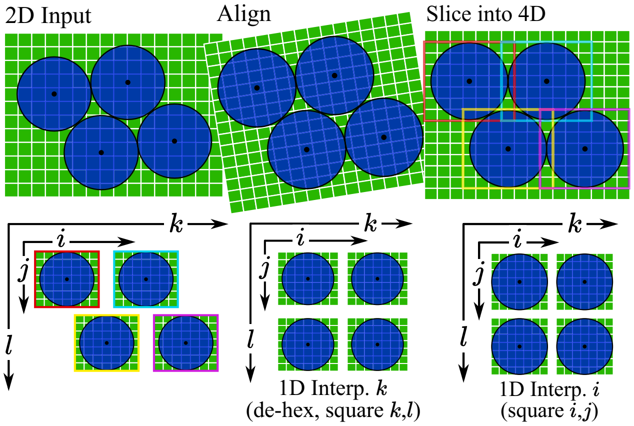

Figure 2. Decoding the raw 2D sensor image to a 4D light field

From the estimated grid parameters there are many potential methods for decoding the lenselet image to a 4D light field. The method we present was chosen for its ease of implementation. The process begins by demosaicing the raw lenselet image, then correcting vignetting by dividing by the white image. At this point the lenselet images, depicted in blue in Fig. 2, are on a non-integer spaced, rotated grid relative to the image's pixels (green). We therefore resample the image, rotating and scaling so all lenselet centers fall on pixel centers, as depicted in the second frame of the figure. The required scaling for this step will not generally be square, and so the resulting pixels are rectangular.

Aligning the lenselet images to an integer pixel grid allows a very simple slicing scheme: the light field is broken into identically sized, overlapping rectangles centered on the lenselet images, as depicted in the top-right and bottom-left frames of Fig. 2. The spacing in the bottom-left frame represents the hexagonal sampling in the lenselet indices k, l, as well as non-square pixels in the pixel indices i, j.

Converting hexagonally sampled data to an orthogonal grid is a well-explored topic; see [2] for a reversible conversion based on 1D filters. We implemented both a 2D interpolation scheme operating in k, l, and a 1D scheme interpolating only along k, and have found the latter approach, depicted in the bottom middle frame of Fig. 2, to be a good approximation. For rectangular lenselet arrays, this interpolation step is omitted. As we interpolate in k to compensate for the hexagonal grid's offsets, we simultaneously compensate for the unequal vertical and horizontal sample rates. The final stage of the decoding process cor-

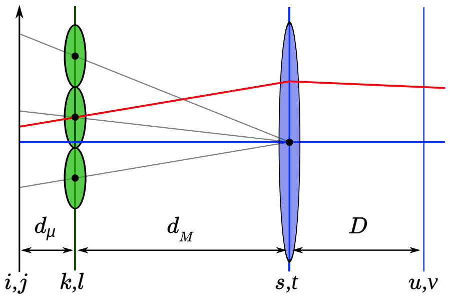

Figure 3. The main lens is modelled as a thin lens and the lenselets as an array of pinholes; gray lines depict lenselet image centers

rects for the rectangular pixels in i, j through a 1D interpolation along i. In every interpolation step we *increase* the effective sample rate in order to avoid loss of information. The final step, not shown, is to mask off pixels that fall outside the hexagonal lenselet image. We denote the result of the decode process the "aligned" light field $L^A(i, j, k, l)$.

4. Pinhole and Thin Lens Model

In this section we derive the relationship between the indices of each pixel and its corresponding spatial ray. Though each pixel of a plenoptic camera integrates light from a volume, we approximate each as integrating along a single ray [8]. We model the main lens as a thin lens, and the lenselets as an array of pinholes, as depicted in Fig. 3. Our starting point is an index resulting from the decoding scheme described above, expressed in homogeneous coordinates $\boldsymbol{n} = [i, j, k, l, 1]$, where k, l are the zero-based absolute indices of the lenselet through which a ray passes, and i, j are the zero-based *relative* pixel indices within each lenselet image. For lenselet images of $N \times N$ pixels, i and j each range from 0 to $N - 1$.

We derive a homogeneous intrinsic matrix $\boldsymbol{H} \in \mathbb{R}^{5\times 5}$ by applying a series of transformations, first converting the index $\boldsymbol{n}$ to a ray representation suitable for ray transfer matrix analysis, then propagating it through the optical system, and finally converting to a light field ray representation. The full sequence of transformations is given by

$$\boldsymbol{\phi}^A = \boldsymbol{H}_{\Phi}^{\phi} \boldsymbol{H}^M \boldsymbol{H}^T \boldsymbol{H}_{\phi}^{\Phi} \boldsymbol{H}_{abs}^{\phi} \boldsymbol{H}_{rel}^{abs} \boldsymbol{n} = \boldsymbol{H}\boldsymbol{n}. \qquad (1)$$

We will derive each component of this process in the 2D plane, starting with the homogenous relative index $\boldsymbol{n}_{2D} = [i, k, 1]$, and later generalize the result to 4D.

The conversion from relative to absolute indices, $\boldsymbol{H}_{rel}^{abs}$ is straightforwardly found from the number of pixels per lenselet N and a translational pixel offset c_{pix} (below). We next convert from absolute coordinates to a light field ray, with the imaging and lenselet planes as the reference planes. We accomplish this using $\boldsymbol{H}_{abs}^{\phi}$,

$$\boldsymbol{H}_{rel}^{abs} = \begin{bmatrix} 1 & N & \text{-}c_{pix} \\ 0 & 1 & 0 \\ 0 & 0 & 1 \end{bmatrix}, \quad \boldsymbol{H}_{abs}^{\phi} = \begin{bmatrix} 1/F_s & 0 & \text{-}c_M/F_s \\ 0 & 1/F_u & \text{-}c_\mu/F_u \\ 0 & 0 & 1 \end{bmatrix}, \quad (2)$$

where F_* and c_* are the spatial frequencies in samples/m, and offsets in samples, of the pixels and lenselets.

Next we express the ray as position and direction via $\boldsymbol{H}_{\phi}^{\Phi}$ (below), and propagate to the main lens using $\boldsymbol{H}^T$:

$$\boldsymbol{H}_{\phi}^{\Phi} = \begin{bmatrix} 1 & 0 & 0 \\ \text{-}1/d_\mu & 1/d_\mu & 0 \\ 0 & 0 & 1 \end{bmatrix}, \quad \boldsymbol{H}^T = \begin{bmatrix} 1 & d_\mu + d_M & 0 \\ 0 & 1 & 0 \\ 0 & 0 & 1 \end{bmatrix}, \qquad (3)$$

where d_* are the lens separations as depicted in Fig. 3. Note that in the conventional plenoptic camera, $d_\mu = f_\mu$, the lenselet focal length.

Next we apply the main lens using a thin lens and small angle approximation (below), and convert back to a light field ray representation, with the main lens as the s, t plane, and the u, v plane at an arbitrary plane separation D:

$$\boldsymbol{H}^M = \begin{bmatrix} 1 & 0 & 0 \\ \text{-}1/f_M & 1 & 0 \\ 0 & 0 & 1 \end{bmatrix}, \quad \boldsymbol{H}_{\Phi}^{\phi} = \begin{bmatrix} 1 & D & 0 \\ 0 & 1 & 0 \\ 0 & 0 & 1 \end{bmatrix}, \qquad (4)$$

where f_M is the focal length of the main lens. Because horizontal and vertical components are independent, extension to 4D is straightforward. Multiplying through Eq. 1 yields an expression for $\boldsymbol{H}$ with twelve non-zero terms:

$$\begin{bmatrix} s \\ t \\ u \\ v \\ 1 \end{bmatrix} = \begin{bmatrix} H_{1,1} & 0 & H_{1,3} & 0 & H_{1,5} \\ 0 & H_{2,2} & 0 & H_{2,4} & H_{2,5} \\ H_{3,1} & 0 & H_{3,3} & 0 & H_{3,5} \\ 0 & H_{4,2} & 0 & H_{4,4} & H_{4,5} \\ 0 & 0 & 0 & 0 & 1 \end{bmatrix} \begin{bmatrix} i \\ j \\ k \\ l \\ 1 \end{bmatrix}. \qquad (5)$$

In a model with pixel or lenselet skew we would expect more non-zero terms. In Section 5 we show that two of these parameters are redundant with camera pose, leaving only 10 free intrinsic parameters.

4.1. Projection Through the Lenselets

We have hidden some complexity in deriving the 4D intrinsic matrix by assuming prior knowledge of the lenselet associated with each pixel. As depicted by the gray lines in Fig. 3, the projected image centers will deviate from the lenselet centers, and as a result a pixel will not necessarily associate with its nearest lenselet. Furthermore, the decoding process presented in Section 3 includes several manipulations which will change the effective camera parameters. By resizing, rotating, interpolating, and centering on the *projected* lenselet images, we have created a virtual light field camera with its own parameters. In this section we compensate for these effects through the application of correction coefficients to the physical camera parameters.

Lenselet-based plenoptic cameras are constructed with careful attention to the coplanarity of the lenselet array and image plane [17]. As a consequence, projection through the lenselets is well-approximated by a single scaling factor, M_{proj}. Scaling and adjusting for hexagonal sampling can similarly be modelled as scaling factors. We therefore correct the pixel sample rates using

$$M_{proj} = [1 + {}^{d_\mu}/_{d_M}]^{\text{-}1}, \quad M_s = N^A/N^S, \quad M_{hex} = {}^2/\sqrt{3},$$
$$F_s^A = M_s M_{proj} F_s^S, \quad F_u^A = M_{hex} F_u^S, \qquad (6)$$

where superscripts indicate that a measure applies to the physical sensor (S), or to the virtual "aligned" camera (A); M_{proj} is derived from similar triangles formed by each gray projection line in Fig. 3; M_s is due to rescaling; and M_{hex} is due to hexagonal/Cartesian conversion. Extension to the vertical dimensions is trivial, omitting M_{hex}.

4.2. Lens Distortion Model

The physical alignment and characteristics of the lenselet array as well as all the elements of the main lens potentially contribute to lens distortion. In the results section we show that the consumer plenoptic camera we employ suffers primarily from directionally dependent radial distortion,

$$\boldsymbol{\theta}^d = \left(1 + k_1 r^2 + k_2 r^4 + \cdots\right)\left(\boldsymbol{\theta}^u - \boldsymbol{b}\right) + \boldsymbol{b},$$
$$r = \sqrt{\theta_s^2 + \theta_t^2}, \quad (7)$$

where $\boldsymbol{b}$ captures decentering, $\boldsymbol{k}$ are the radial distortion coefficients, and $\boldsymbol{\theta}^u$ and $\boldsymbol{\theta}^d$ are the undistorted and distorted 2D ray directions, respectively. Note that we apply the small angle assumption, such that $\boldsymbol{\theta} \approx [dx/dz, dy/dz]$. We define the complete distortion vector as $\boldsymbol{d} = [\boldsymbol{b}, \boldsymbol{k}]$. Extension to more complex distortion models is left as future work.

5. Calibration and Rectification

The plenoptic camera gathers enough information to perform calibration from unstructured and unknown environments. However, as a first pass we take a more conventional approach familiar from projective camera calibration [10, 24], in which the locations of a set of 3D features are known – we employ the corners of a checkerboard pattern of known dimensions, with feature locations expressed in the frame of reference of the checkerboard. As depicted in Fig. 4a, projective calibration builds an objective function from the 2D distance between observed and expected projected feature locations, $\boldsymbol{n}$ and $\hat{\boldsymbol{n}}$, forming the basis for optimization over the camera's poses and intrinsics.

Plenoptic calibration is complicated by the fact that a single feature will appear in the imaging plane multiple times, as depicted in Fig. 4b. A tempting line of reasoning is to again formulate an error metric based on the 2D distance between observed and expected feature locations. The problem arises that the observed and expected features do not generally appear in the same lenselet images – indeed the number of expected and observed features is not generally equal. As such, a meaningful way of finding the "closest" distance between each observation and the set of expected features is required. We propose two practical methods. In the first, each known 3D feature location $\boldsymbol{P}$ is transformed to its corresponding 4D light field plane $\boldsymbol{\lambda}$ using the point-plane correspondence [5]. The objective function is then taken as the point-to-plane distance between each observation $\boldsymbol{n}$ and the plane $\boldsymbol{\lambda}$. The second approach generates a projected ray $\hat{\boldsymbol{\phi}}$ from each observation $\boldsymbol{n}$. The error metric, which we denote the "ray reprojection error", is taken as the point-to-ray distance between $\hat{\boldsymbol{\phi}}$ and $\boldsymbol{P}$, as depicted in Fig. 4b. The two methods are closely related, and we pursue the second, as it is computationally simpler.

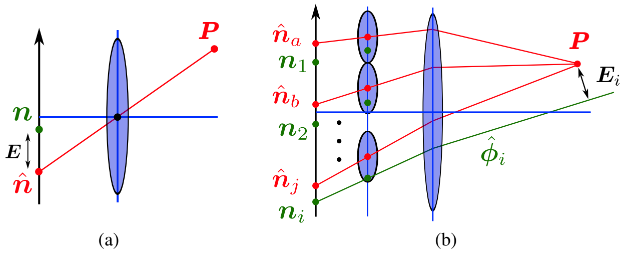

Figure 4. In conventional projective calibration (a) a 3D feature $\boldsymbol{P}$ has one projected image, and a convenient error metric is the 2D distance between the expected and observed image locations $|\hat{\boldsymbol{n}} - \boldsymbol{n}|$. In the plenoptic camera (b) each feature has multiple expected and observed images $\hat{\boldsymbol{n}}_j, \boldsymbol{n}_i \in \mathbb{R}^4$, which generally do not appear beneath the same lenselets; we propose the per-observation ray reprojection metric $|\boldsymbol{E}_i|$ taken as the 3D distance between the reprojected ray $\hat{\boldsymbol{\phi}}_i$ and the feature location $\boldsymbol{P}$.

The observed feature locations are extracted by treating the decoded light field from Section 3 as an array of $N_i \times N_j$ 2D images in k and l, applying a conventional feature detection scheme [11] to each. If the plenoptic camera takes on M poses in the calibration dataset and there are n_c features on the calibration target, the total feature set over which we optimize is of size $n_c M N_i N_j$. Our goal is to find the intrinsic matrix $\boldsymbol{H}$, camera poses $\boldsymbol{T}$, and distortion parameters $\boldsymbol{d}$ which minimize the error across all features,

$$\underset{\boldsymbol{H},\boldsymbol{T},\boldsymbol{d}}{\operatorname{argmin}} \sum_{c=1}^{n_c} \sum_{m=1}^{M} \sum_{s=1}^{N_i} \sum_{t=1}^{N_j} ||\hat{\boldsymbol{\phi}}_c^{s,t}(\boldsymbol{H}, \boldsymbol{T}_m, \boldsymbol{d}), \boldsymbol{P}_c||^{\text{pt-ray}}, \quad (8)$$

where $||\cdot||^{\text{pt-ray}}$ is the ray reprojection error described above.

Each of the M camera poses has 6 degrees of freedom, and from Eq. 5 the intrinsic model $\boldsymbol{H}$ has 12 free parameters. However, there is a redundancy between $H_{1,5}, H_{2,5}$, which effect horizontal translation within the intrinsic model, and the translational components of the poses $\boldsymbol{T}$. Were this redundancy left in place, the intrinsic model could experience unbounded translational drift and fail to converge. We therefore force the intrinsic parameters $H_{1,5}$ and $H_{2,5}$ such that pixels at the center of i, j map to rays at $s, t = 0$. Because of this forcing, the physical location of $s, t = 0$ on the camera will remain unknown, and if it is required must be measured by alternative means.

The number of parameters over which we optimize is now reduced to 10 for intrinsics, 5 for lens distortion, and 6 for each of the M camera poses, for a total of $6M + 15$. Note the significant simplification relative to multiple-camera approaches, which grow with sample count in i and j – this is discussed further in Results.

As in monocular camera calibration, a Levenberg-Marquardt or similar optimization algorithm can be employed which exploits knowledge of the Jacobian. Rather than deriving the Jacobian here we describe its sparsity pattern and show results based on the trust region reflective algorithm implemented in MATLAB's `lsqnonlin` function [3]. In practice we have found this to run quickly on modern hardware, finishing in tens of iterations and taking in the order of minutes to complete.

The Jacobian sparsity pattern is easy to derive: each of the M pose estimates will only influence that pose's $n_c N_i N_j$ error terms, while all of the 15 intrinsic and distortion parameters will affect every error term. As a practical example, for a checkerboard with 256 corners, viewed from 16 poses by a camera with $N_i = N_j = 8$ spatial samples, there will be $N_e = n_c M N_i N_j = (16)(8)(8)(256) = 262{,}144$ error terms and $N_v = 6M + 15 = 123$ optimization variables. Of the $N_e N_v = 32{,}243{,}712$ possible interactions, $(15+6)N_e = 5{,}505{,}024$, or about 17% will be non-zero.

5.1. Initialization

The calibration process proceeds in stages: first initial pose and intrinsic estimates are formed, then an optimization is carried out with no distortion parameters, and finally a full optimization is carried out with distortion parameters. To form initial pose estimates, we again treat the decoded light fields across M poses each as an array of $N_i \times N_j$ 2D images. By passing all the images through a conventional camera calibration process, for example that proposed by Heikkilä [10], we obtain a *per-image* pose estimate. Taking the mean or median within each light field's $N_i \times N_j$ per-image pose estimates yields M *physical* pose estimates. Note that distortion parameters are excluded from this process, and the camera intrinsics that it yields are ignored.

In Section 4 we derived a closed-form expression for the intrinsic matrix $\boldsymbol{H}$ based on the plenoptic camera's physical parameters and the parameters of the decoding process (1), (6). We use these expressions to form the initial estimate of the camera's intrinsics. We have found the optimization process to be insensitive to errors in these initial estimates, and in cases where the physical parameters of the camera are unknown, rough estimates may suffice. Automatic estimation of the initial parameters is left as future work.

5.2. Rectification

We wish to rectify the light field imagery, reversing the effects of lens distortion and yielding square pixels in i, j and k, l. Our approach is to interpolate from the decoded light field L^A at a set of continuous-domain indices $\tilde{\boldsymbol{n}}^A$ such that the interpolated light field approximates a distortion-free rectified light field L^R. In doing so, we must select an *ideal* intrinsic matrix $\boldsymbol{H}^R$, bearing in mind that deviating too far from the physical camera parameters will yield black pixels near the edges of the captured light field, where no information is available. At the same time, we wish to force horizontal and vertical sample rates to be equal – i.e. we wish to force $H_{1,1} = H_{2,2}$, $H_{1,3} = H_{2,4}$, $H_{3,1} = H_{4,2}$ and $H_{3,3} = H_{4,4}$. As a starting point, we replace each of these four pairs with the mean of its members, simultaneously readjusting $H_{1,5}$ and $H_{2,5}$ so as to maintain the centering described earlier.

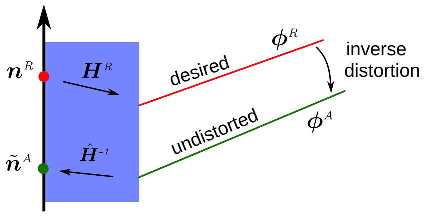

Figure 5. Reversing lens distortion: tracing from the desired pixel location $\boldsymbol{n}^R$ through the ideal optical system, reversing lens distortion, then returning through the physical optical system to the measured pixel $\tilde{\boldsymbol{n}}^A$

The rectification process is depicted in Fig. 5, with the optical system treated as a black box. To find $\tilde{\boldsymbol{n}}^A$ we begin with the indices of the rectified light field $\boldsymbol{n}^R$, and project through the ideal optical system by applying $\boldsymbol{H}^R$, yielding the ideal ray $\boldsymbol{\phi}^R$. Referring to the distortion model (7), the desired ray $\boldsymbol{\phi}^R$ is arrived at by applying the forward model to some unknown undistorted ray $\boldsymbol{\phi}^A$. Assuming we can find $\boldsymbol{\phi}^A$, shown below, the desired index $\tilde{\boldsymbol{n}}^A$ is arrived at by applying the inverse of the estimated intrinsic matrix $\hat{\boldsymbol{H}}^{-1}$.

There is no closed-form solution to the problem of reversing the distortion model (7), and so we propose an iterative approach similar to that of Melen [15]. Starting with an estimate of r taken from the desired ray $\boldsymbol{\phi}^R$, we solve for the first-pass estimate $\boldsymbol{\phi}_1^A$ using (7), then update r from the new estimate and iterate. In practice we have found as few as two iterations to produce acceptable results.

6. Results

We carried out calibration on five datasets collected with the commercially available Lytro plenoptic camera. The same camera was used for all datasets, but the optical configuration was changed between datasets by adjusting the camera's focal settings – care was taken not to change settings within a dataset.

Three calibration grids of differing sizes were used: a 19 × 19 grid of 3.61 mm cells, a 19 × 19 grid of 7.22 mm cells, and an 8 × 6 grid of 35.1 × 35.0 mm cells. Images within each dataset were taken over a range of depths and orientations. In Datasets A and B, range did not exceed 20 cm, in C and D it did not exceed 50 cm, and in E it did not exceed 2 m. Close ranges were favoured in all datasets so as to maximize accuracy in light of limited effective baseline

Table 1. Virtual “Aligned” Camera Parameters

Parameter	Value
N	10 pix
F_s, F_u	716,790, 71,950 samp/m
c_M, c_μ, c_{pix}	1,645.3, 164.7, 6 samp
d_M, d_μ, f_M	6.6506, 0.025, 6.45 mm

Table 2. Estimated Parameters, Dataset B

Parameter	Initial	Intrinsics	Distortion
$H_{1,1}$	3.6974e-04	3.7642e-04	4.0003e-04
$H_{1,3}$	-8.6736e-19	-5.6301e-05	-9.3810e-05
$H_{1,5}$	-1.5862e-03	8.8433e-03	1.5871e-02
$H_{2,2}$	3.6974e-04	3.7416e-04	3.9680e-04
$H_{2,4}$	-8.6736e-19	-5.3831e-05	-9.3704e-05
$H_{2,5}$	-1.5862e-03	8.3841e-03	1.5867e-02
$H_{3,1}$	-1.5194e-03	-1.1888e-03	-1.1833e-03
$H_{3,3}$	1.8167e-03	1.7951e-03	1.8105e-03
$H_{3,5}$	-3.3897e-01	-3.3681e-01	-3.3175e-01
$H_{4,2}$	-1.5194e-03	-1.1657e-03	-1.1583e-03
$H_{4,4}$	1.8167e-03	1.7830e-03	1.8077e-03
$H_{4,5}$	-3.3897e-01	-3.2501e-01	-3.2230e-01
b_1	.	.	1.5258e-01
b_2	.	.	-1.1840e-01
k_1	.	.	2.9771e+00
k_2	.	.	-3.4308e-03
k_3	.	.	-5.5949e-03

Table 3. RMS Ray Reprojection Error (mm)

Dataset/grid	Initial	Intrin.	Dist.	Multi$_{295}$	Multi$_{631}$
A/3.61	3.20	0.146	0.0835	0.198	0.109
B/3.61	5.06	0.148	0.0628	0.178	0.0682
C/7.22	8.63	0.255	0.106	0.220	0.107
D/7.22	5.92	0.247	0.105	0.382	0.108
E/35.1	13.8	0.471	0.363	2.22	0.336

in the s, t plane. This did not limit the applicability of each calibration to longer-range imagery.

The datasets each contained between 10 and 18 poses, and are available online[1]. Investigating the minimum number of poses required to obtain good calibration results is left as future work, but from the results obtained it is clear that 10 is sufficient for appropriately diverse poses.

The decoding process requires a white image for locating lenselet image centers and correcting for vignetting. For this purpose, we used white images provided with the camera. Fig. 7a shows a crop of a typical white image, with the grid model overlaid. A closeup of one of the checkerboard images after demosaicing and correcting for vignetting is shown in Fig. 7b. We decoded to a 10-pixel aligned intermediary image yielding, after interpolations, $11 \times 11 \times 380 \times 380$ pixels. We ignored a border of two pixels in i, j due to demosaicing and edge artefacts.

An initial estimate of the camera's intrinsics was formed from its physical parameters, adjusted to reflect the parameters of the decode process using Eq. 6. The adjusted parameters for Dataset B are shown in Table 1, and the resulting intrinsics appear in the “Initial” column of Table 2.

For feature detection we used the Robust Automatic Detection Of Calibration Chessboards [11] toolbox[2]. All features appear in all images, simplifying the task of associating them. Each calibration stage converged within 15 iterations in all cases, with the longer-range datasets generally taking longer to converge. Table 2 shows the estimated parameters for Dataset B at the three stages of the calibration process: initial estimate, intrinsics without distortion, and intrinsics with distortion. Table 3 summarizes the root mean square (RMS) ray reprojection error, as described in Section 5, at the three calibration stages and across the five datasets. Results are also shown for two conventional multiple-camera calibration models, Multi$_{295}$ and Multi$_{631}$. The first represents the plenoptic camera as an array of projective sub-cameras with independent relative poses and identical intrinsics and distortion parameters, while the second also includes per-sub-camera intrinsic and distortion parameters. Both camera array models grow in complexity with sample count in i and j, and for 7×7 samples require 295 and 631 parameters, respectively.

From Table 3, the Multi$_{295}$ model performs poorly, while Multi$_{631}$ approaches the performance of our proposed 15-parameter model. Referring to Table 2, we observe that the calibrated $H_{1,3}$ and $H_{2,4}$ terms converged to nonzero values. These represent the dependence of a ray's position on the lenselet through which it passes, and a consequence of these nonzero values is that rays take on a wide variety of rational-valued positions in the s, t plane. This raises an important problem with the multiple-camera models, which unrealistically constrain rays to pass through a small set of sub-camera apertures, rather than allowing them to vary smoothly in position. We take this to explain the poor performance of the Multi$_{295}$ model. The Multi$_{631}$ model performed well despite this limitation, which we attribute to its very high dimensionality. Aside from the obvious tradeoff in complexity – compare with our proposed 15-parameter model – this model presents a risk of overfitting and correspondingly reduced generality.

Fig. 6 depicts typical ray reprojection error in our proposed model as a function of direction and position. The top row depicts error with no distortion model, and clearly shows a radial pattern as a function of both direction (left) and position (right). The bottom row shows error with the proposed distortion model in place – note the order of magnitude reduction in the error scale, and the absence of any evident radial pattern. This shows the proposed distortion model to account for most lens distortion for this camera.

We have carried out decoding and rectification on a wide range of images – more than 700 at the time of writing.

[1] http://marine.acfr.usyd.edu.au/permlinks/Plenoptic

[2] http://www-personal.acfr.usyd.edu.au/akas9185/AutoCalib/AutoCamDoc/index.html

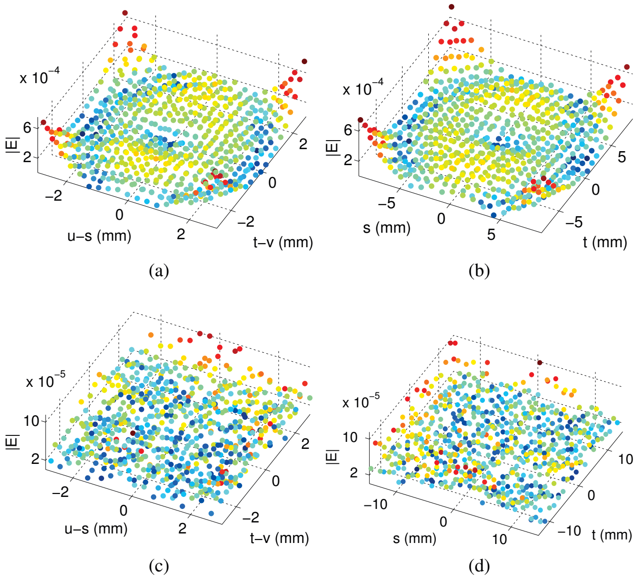

(a) (b)

(c) (d)

Figure 6. Ray reprojection error for Dataset B. Left: error vs. ray direction; right: error vs. ray position; top: no distortion model; bottom: the proposed five-parameter distortion model – note the order of magnitude difference in the error scale. The proposed model has accounted for most lens distortion for this camera.

Examples of decoded and rectified light fields are shown in Figs. 7c–h, as 2D slices in k, l – i.e. with i and j fixed – and further examples are available online. Rectification used a four-iteration inverse distortion model. The straight red rulings aid visual confirmation that rectification has significantly reduced the effects of lens distortion. The two last images are also shown in Fig. 8 as slices in the horizontal i, k plane passing through the center of the lorikeet's eye. The straight lines display minimal distortion, and that they maintain their slopes confirms that rectification has not destroyed the 3D information captured by the light field.

7. Conclusions and Future Work

We have presented a 15-parameter camera model and method for calibrating a lenselet-based plenoptic camera. This included derivation of a novel physically based 4D intrinsic matrix and distortion model which relate the indices of a pixel to its corresponding spatial ray. We proposed a practical objective function based on ray reprojection, and presented an optimization framework for carrying out calibration. We also presented a method for decoding hexagonal lenselet-based plenoptic images without prior knowledge of the camera's parameters, and related the resulting images to the camera model. Finally, we showed a method for rectifying the decoded images, reversing the effects of lens distortion and yielding square pixels in i, j and k, l. In the rectified images, the ray corresponding to each pixel is easily found through a single matrix multiplication (5).

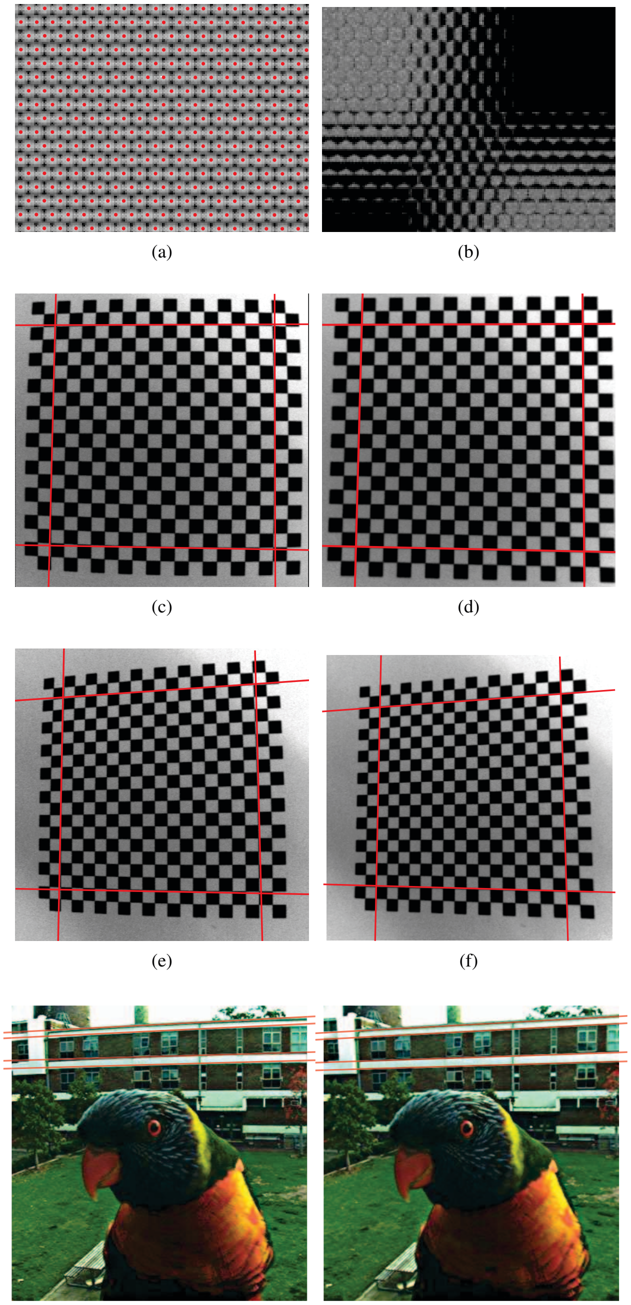

(a) (b)

(c) (d)

(e) (f)

(g) (h)

Figure 7. a) Crop of a white image overlaid with the estimated grid, and b) the demosaiced and vignetting-corrected raw checkerboard image; c–h) examples of (left) unrectified and (right) rectified light fields; red rulings aid confirmation that rectification has significantly reduced the effect of lens distortion.

Validation included five datasets captured with a commercially available plenoptic camera, over three calibration grid sizes. Typical RMS ray reprojection errors were 0.0628, 0.105 and 0.363 mm for 3.61, 7.22 and 35.1 mm calibration grids, respectively. Real-world rectified imagery

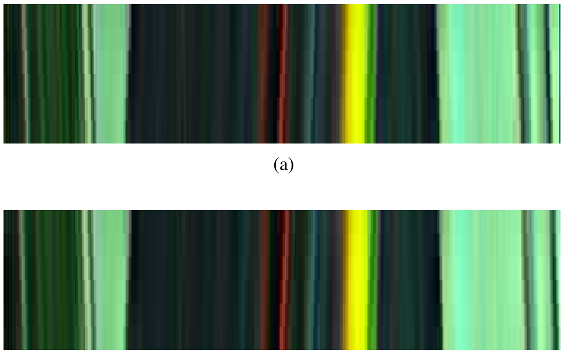

(a)

(b)

Figure 8. Slices in the horizontal plane i, k of the a) unrectified and b) rectified lorikeet images from Figs. 7g and h; i is on the vertical axis, and k on the horizontal

demonstrated a significant reduction in lens distortion. Future work includes automating initial estimation of the camera's physical parameters, more complex distortion models, and autocalibration from arbitrary scenes.

Acknowledgments This work is supported in part by the Australian Research Council (ARC), the New South Wales State Government, the Australian Centre for Field Robotics, The University of Sydney, and the Australian Government's International Postgraduate Research Scholarship (IPRS).

References

[1] T. Bishop and P. Favaro. The light field camera: Extended depth of field, aliasing, and superresolution. *Pattern Analysis and Machine Intelligence, IEEE Trans. on*, 34(5):972–986, May 2012.

[2] L. Condat, B. Forster-Heinlein, and D. Van De Ville. H2O: reversible hexagonal-orthogonal grid conversion by 1-D filtering. In *Image Processing, 2007. ICIP 2007. IEEE Intl. Conference on*, volume 2, pages II–73. IEEE, 2007.

[3] A. Conn, N. Gould, and P. Toint. *Trust region methods*, volume 1. Society for Industrial Mathematics, 1987.

[4] D. G. Dansereau, D. L. Bongiorno, O. Pizarro, and S. B. Williams. Light field image denoising using a linear 4D frequency-hyperfan all-in-focus filter. In *Proceedings SPIE Computational Imaging XI*, page 86570P, Feb 2013.

[5] D. G. Dansereau and L. T. Bruton. A 4-D dual-fan filter bank for depth filtering in light fields. *IEEE Trans. on Signal Processing*, 55(2):542–549, 2007.

[6] D. G. Dansereau, I. Mahon, O. Pizarro, and S. B. Williams. Plenoptic flow: Closed-form visual odometry for light field cameras. In *Intelligent Robots and Systems (IROS), IEEE/RSJ Intl. Conf. on*, pages 4455–4462. IEEE, Sept 2011.

[7] T. Georgiev, A. Lumsdaine, and S. Goma. Plenoptic principal planes. In *Computational Optical Sensing and Imaging*. Optical Society of America, 2011.

[8] M. Grossberg and S. Nayar. The raxel imaging model and ray-based calibration. *International Journal of Computer Vision*, 61(2):119–137, 2005.

[9] M. Harris. Focusing on everything – light field cameras promise an imaging revolution. *IEEE Spectrum*, 5:44–50, 2012.

[10] J. Heikkilä and O. Silvén. A four-step camera calibration procedure with implicit image correction. In *Computer Vision and Pattern Recognition (CVPR), IEEE Conference on*, pages 1106–1112. IEEE, 1997.

[11] A. Kassir and T. Peynot. Reliable automatic camera-laser calibration. In *Australasian Conference on Robotics and Automation*, 2010.

[12] R. Koch, M. Pollefeys, L. Van Gool, B. Heigl, and H. Niemann. Calibration of hand-held camera sequences for plenoptic modeling. In *ICCV*, volume 1, pages 585–591. IEEE, 1999.

[13] D. Lanman. *Mask-based Light Field Capture and Display*. PhD thesis, Brown University, 2012.

[14] A. Lumsdaine and T. Georgiev. The focused plenoptic camera. In *Computational Photography (ICCP), IEEE Intl. Conference on*, pages 1–8. IEEE, 2009.

[15] T. Melen. *Geometrical modelling and calibration of video cameras for underwater navigation*. Institutt for Teknisk Kybernetikk, Universitetet i Trondheim, Norges Tekniske Høgskole, 1994.

[16] R. Ng. Fourier slice photography. In *ACM Trans. on Graphics (TOG)*, volume 24, pages 735–744. ACM, Jul 2005.

[17] R. Ng, M. Levoy, M. Brédif, G. Duval, M. Horowitz, and P. Hanrahan. Light field photography with a hand-held plenoptic camera. *Computer Science Technical Report CSTR*, 2, 2005.

[18] T. Svoboda, D. Martinec, and T. Pajdla. A convenient multicamera self-calibration for virtual environments. *Presence: Teleoperators & Virtual Environments*, 14(4):407–422, 2005.

[19] V. Vaish, M. Levoy, R. Szeliski, C. Zitnick, and S. Kang. Reconstructing occluded surfaces using synthetic apertures: Stereo, focus and robust measures. In *Computer Vision and Pattern Recognition (CVPR), IEEE Conference on*, volume 2, pages 2331–2338. IEEE, 2006.

[20] V. Vaish, B. Wilburn, N. Joshi, and M. Levoy. Using plane + parallax for calibrating dense camera arrays. In *Computer Vision and Pattern Recognition (CVPR), IEEE Conference on*, volume 1, pages I–2. IEEE, 2004.

[21] B. Wilburn, N. Joshi, V. Vaish, E. Talvala, E. Antunez, A. Barth, A. Adams, M. Horowitz, and M. Levoy. High performance imaging using large camera arrays. *ACM Trans. on Graphics (TOG)*, 24(3):765–776, 2005.

[22] Z. Xu, J. Ke, and E. Lam. High-resolution lightfield photography using two masks. *Optics Express*, 20(10):10971–10983, 2012.

[23] Z. Yu, J. Yu, A. Lumsdaine, and T. Georgiev. An analysis of color demosaicing in plenoptic cameras. In *Computer Vision and Pattern Recognition (CVPR), IEEE Conference on*, pages 901–908. IEEE, 2012.

[24] Z. Zhang. A flexible new technique for camera calibration. *Pattern Analysis and Machine Intelligence, IEEE Trans. on*, 22(11):1330–1334, 2000.